NJC

PAPER

View Article Online
View Journal | View Issue

Cite this: *New J. Chem.*, 2017, **41**, 13553

Facile synthesis of porous iron oxide/graphene hybrid nanocomposites and potential application in electrochemical energy storage†

Jiakang Min,[ab] Krzysztof Kierzek,[c] Xuecheng Chen,*[ad] Paul K. Chu,[e] Xi Zhao,*[f] Ryszard J. Kaleńczuk,[d] Tao Tang*[a] and Ewa Mijowska[d]

Received 8th September 2017,
Accepted 3rd October 2017

DOI: 10.1039/c7nj03416d

rsc.li/njc

A facile and efficient method is used to synthesize porous iron oxide coated with graphene as electrode materials for lithium-ion batteries and supercapacitors. Graphene encapsulation of porous Fe_2O_3 and Fe_3O_4 nanorods is directly carried out from FeOOH@GO colloids by taking advantage of an electrostatic self-assembly method, owing to the positively-charged surface of FeOOH and the negatively-charged surface of GO. The combination of graphene and porous iron oxide brings about multifunctional features of the electrode materials as follows: (1) enhanced electrical conductivity makes the electrodes the current collectors; (2) reinforced softness of the electrodes accommodates the large volume changes during charge–discharge cycles; (3) improved high specific surface area of the electrodes increases the accessibility of the active electrode materials to electrolyte; (4) the pores formed by graphene and iron oxide particles facilitate ion transportation; (5) iron oxide particles separate graphene and prevent their restacking or agglomeration, and *vice versa*, thus improving the immersion and splitting of electrolyte into and out of the electroactive material. Consequently, the porous iron oxide/graphene hybrid nanocomposites deliver a good performance in the electrochemical energy storage for lithium-ion batteries and supercapacitors.

Introduction

The renewable energy obtained from solar, wind, and hydro sources is becoming prevalent as a substitute for fossil fuels due to the growing demand for green energy worldwide. However, they may not be accessible everywhere and it is important to find different modes to store the energy efficiently and use it timely. Since rechargeable lithium-ion batteries (LIBs) and supercapacitors are two of the most popular energy storage devices, particularly for portable electronics, mobile communication devices, electric cars and so on, numerous fundamental studies for the development of advanced LIBs and supercapacitors have been conducted.[1,2] In principle, the ideal electrode materials should be economical, non-toxic, environment-friendly, robust, naturally abundant, corrosion-resistant, durable and flame retardant while possessing large energy and power densities and good cycling characteristics.[3,4]

Iron oxide is promising in energy storage due to its high theoretical capacity (924 mA h g^{-1}), natural abundance, low-cost, good chemical stability, and environmental friendliness.[5–8] However, iron oxide anodes suffer from poor cycling performance on account of low conductivity and morphology collapse as a result of the large volume change during charging and discharging.[9] In this respect, nanoscale materials are preferred because the small size can partially buffer the stress and strain induced by volume expansion or contraction.[10–12] For example, Zhou *et al.* prepared nano Fe_2O_3 decorated with single-walled carbon nanotubes (SWCNT) as flexible anodes in LIBs, boasting a discharge capacity of 801 mA h g^{-1} after 90 cycles. The highly conducting SWCNT network in the membrane not only facilitates the electron conduction in Fe_2O_3, but also buffers the strain of the materials.[13] The other strategy is to store the active materials in hollow spheres to ease the volume change of iron oxide.[14] The use of carbon coatings on iron oxide is also one of the most effective ways to prepare

[a] *State Key Laboratory of Polymer Physics and Chemistry, Changchun Institute of Applied Chemistry, Chinese Academy of Science, Renmin Road 5625, 130022, Changchun, China. E-mail: ttang@ciac.ac.cn*
[b] *University of Chinese Academy of Sciences, Beijing 100039, China*
[c] *Department of Polymer and Carbonaceous Materials, Wroclaw University of Technology, ul. Gdanska 7/9, 50344 Wroclaw, Poland*
[d] *Nanomaterials Physicochemistry Department, Faculty of Chemical Technology and Engineering, West Pomeranian University of Technology Szczecin, al. Piastów 45, 70-311 Szczecin, Poland*
[e] *Department of Physics and Materials Science, City University of Hong Kong, Tat Chee Avenue, Kowloon, Hong Kong, China*
[f] *Institute of Theoretical Chemistry, State Key Lab Theoretical & Computation Chemistry, Jilin University, Changchun 130023, China. E-mail: xchen@ciac.ac.cn, zhaoxi@jlu.edu.cn*

† Electronic supplementary information (ESI) available. See DOI: 10.1039/c7nj03416d

high-performance electrode materials.[15] For instance, various carbon/Fe_3O_4 anode materials with good electrochemical performance,[16–19] including Fe_3O_4 nanospheres, nanospindles, and nanowires with carbon shells,[20–24] iron oxide nanoparticles coated with graphene with excellent properties in LIBs,[25,26] have been reported. However, the previous synthesis methods are relatively complicated and time-consuming. An easier and more convenient method can broaden the use of iron oxide in LIBs. Recently, the combination of Fe_3O_4 nanoparticles with conductive carbon materials can significantly decrease the resistance of the hybrid materials, making it an ideal candidate for supercapacitor electrode materials.[27–31] However, the most reported results were obtained by a three-electrode system; a two-electrode system was seldom used. To further improve the application of porous iron oxide based carbon materials in a supercapacitor, we evaluated the obtained porous iron oxide samples in real conditions using the two-electrode system.

Herein, porous Fe_2O_3 and Fe_3O_4 nanorods coated with graphene (GNS) are prepared from FeOOH@GO colloids by taking advantage of an electrostatic self-assembly method, owing to the positively-charged surface of FeOOH and the negatively-charged surface of GO. The combination of graphene and iron oxide brings about multifunctional features of the electrode materials as follows: (1) enhanced electrical conductivity makes the electrodes the current collectors; (2) reinforced softness of electrodes accommodates the large volume changes during charge–discharge cycles; (3) improved high specific surface area of electrodes increases the accessibility of the active electrode materials to electrolyte; (4) the pores formed by graphene and iron oxide particles facilitate ion transportation; (5) iron oxide particles separate graphene and prevent their restacking or agglomeration, and *vice versa*, thus improving the immersion and splitting of electrolyte into and out of the electroactive material, leading to improved electrochemical characteristics. Consequently, the porous iron oxide/graphene hybrid nanocomposites deliver a good performance in the electrochemical energy storage for lithium-ion batteries and supercapacitors.

Results and discussion

As presented in Scheme 1, first, the synthesized spindle-shaped FeOOH nanorods were mixed with a GO solution, and then GO-coated FeOOH nanorods colloids (as shown in Fig. S1, ESI†) were formed by *via* an electrostatic self-assembly method, owing to the positive charges on the surface of FeOOH and the negative charges on the surface of GO. After the drying and

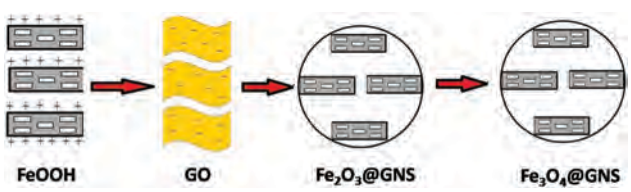

Scheme 1 Schematic of the synthesis of iron oxide nanorods coated with graphene.

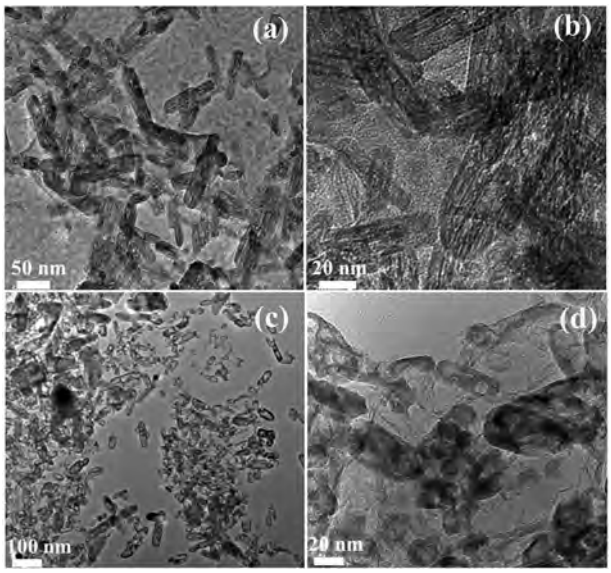

Fig. 1 TEM images: (a and b) porous Fe_2O_3@GNS nanocomposite and (c and d) porous Fe_3O_4@GNS nanocomposite fabricated by electrostatic self-assembly.

reduction process, Fe_2O_3@GNS was obtained. Second, Fe_2O_3@GNS was further annealed at 450 °C for 2 h under Ar to reduce the Fe_2O_3 spindle to Fe_3O_4 *in situ*, and then Fe_3O_4@GNS nanocomposite was obtained. The structural details of Fe_2O_3@GNS and Fe_3O_4@GNS revealed by TEM are displayed in Fig. 1. The morphology of Fe_2O_3@GNS (Fig. 1a, b) and Fe_3O_4@GNS (Fig. 1c, d) is similar, showing several black nanorods randomly distributed on graphene flakes. Fig. 1b and Fig. S2 (ESI†) are the HRTEM images, showing hollow space in Fe_2O_3 nanorods, and Fig. 1d depicts the HRTEM image of Fe_3O_4 nanorods coated with graphene with much more hollow space.

The SEM images of Fe_2O_3@GNS and Fe_3O_4@GNS are shown in Fig. 2. No big spheres appeared, as shown in Fig. 2a and c, and graphene coated iron oxide relatively well, which is consistent with the TEM results (Fig. 1). As indicated by red arrows, Fe_2O_3 and

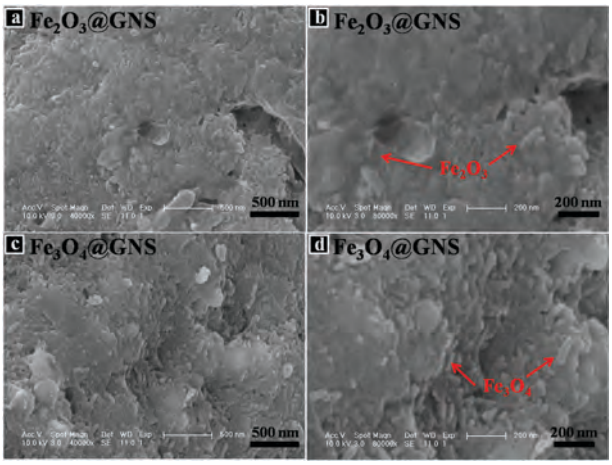

Fig. 2 SEM images of (a and b) Fe_2O_3@GNS and (c and d) Fe_3O_4@GNS samples.

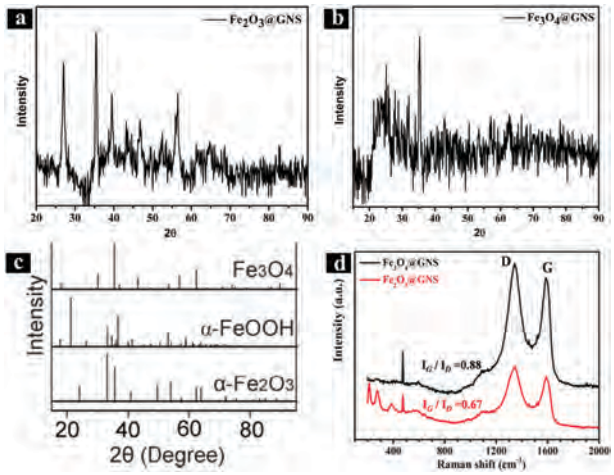

Fig. 3 (a–c) XRD patterns of porous Fe_2O_3@GNS and Fe_3O_4@GNS. (d) Raman spectra of porous Fe_2O_3@GNS and Fe_3O_4@GNS.

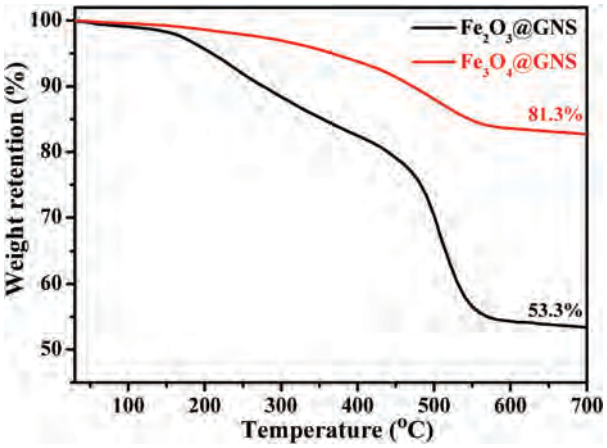

Fig. 4 TGA profiles of Fe_2O_3@GNS and Fe_3O_4@GNS under an air flow.

Fe_3O_4 nanorods are visible in Fig. 2b and d, respectively. The elemental mapping of FeOOH@GO, Fe_2O_3@GNS and Fe_3O_4@GNS shows the uniform distribution of Fe, C and O in these materials (Fig. S3a–c, ESI†).

The X-ray diffraction (XRD) patterns of Fe_2O_3@GNS and Fe_3O_4@GNS and their standard XRD patterns are exhibited in Fig. 3a–c. The strong peak at 2θ = 26° and the broad ones at 43.3° correspond to the characteristic (002) and (100) diffraction planes of the reduced graphene, respectively. The other peaks at 27°, 33°, 36°, 40°, 48° and 56° are ascribed to α-Fe_2O_3 (JCPDS No. 33-0664, Fig. 3a and c), confirming that the nanorods observed by TEM are α-Fe_2O_3. After annealing in Ar at 450 °C, new diffraction peaks at 2θ = 18°, 30°, 43°, and 63° emerge, indicating that most of Fe_2O_3 is reduced to Fe_3O_4 (JCPDS No. 19-0629, Fig. 3b and c). The X-ray photoelectron spectroscopy (XPS) results of the iron element in Fe_2O_3@GNS and Fe_3O_4@GNS are displayed in Fig. S3d (ESI†). XPS can be used to determine the oxidation state of iron because the core electron lines of ferrous and ferric ions can both be detected and distinguished in the spectra. Raman analysis was also used to evaluate the obtained samples. As shown in Fig. 3d, there are two typical peaks at 1340 and 1585 cm^{-1} ascribed to the D and G bands of graphene. As ca be observed from the ratio of I_G/I_D, graphene in Fe_2O_3@GNS (I_G/I_D = 0.67) has more defects than that in Fe_3O_4@GNS (I_G/I_D = 0.88) because of the heat treatment on Fe_3O_4@GNS. When we compared Fe_2O_3@GNS (red line) and Fe_3O_4@GNS (black line), it was observed that there was a trace amount of Fe_2O_3 in Fe_3O_4@GNS. Most of Fe_2O_3 was found to be reduced to Fe_3O_4 by graphene through the heat treatment. TGA was used to determine the weight loss of Fe_2O_3@GNS and Fe_3O_4@GNS under ambient incineration conditions. As shown in Fig. 4, the weight loss from graphene takes place mainly between 200 and 700 °C and Fe_2O_3@GNS begins to pyrolyze at 190 °C under an air flow. After annealing in Ar, the stability of Fe_3O_4@GNS is enhanced with respect to Fe_2O_3@GNS, and Fe_3O_4@GNS begins to decompose at 200 °C under an air flow. The difference in the decomposition temperature between Fe_2O_3@GNS and Fe_3O_4@GNS stems from the functional groups in GNS. The iron oxide content in Fe_2O_3@GNS and Fe_3O_4@GNS is 53.3 and 78.6 wt% (81.3 wt% after oxidation at 700 °C), respectively. To investigate the porosity of Fe_2O_3@GNS and Fe_3O_4@GNS, N_2 sorption/desorption isotherms are obtained. Fig. 5 displays the typical II isotherms of hysteresis of the porous Fe_2O_3@GNS and Fe_3O_4@GNS. Based on the analysis of the adsorption branch of nitrogen sorption, the specific surface areas (Brunauer–Emmett–Teller, (BET)) of Fe_2O_3@GNS and

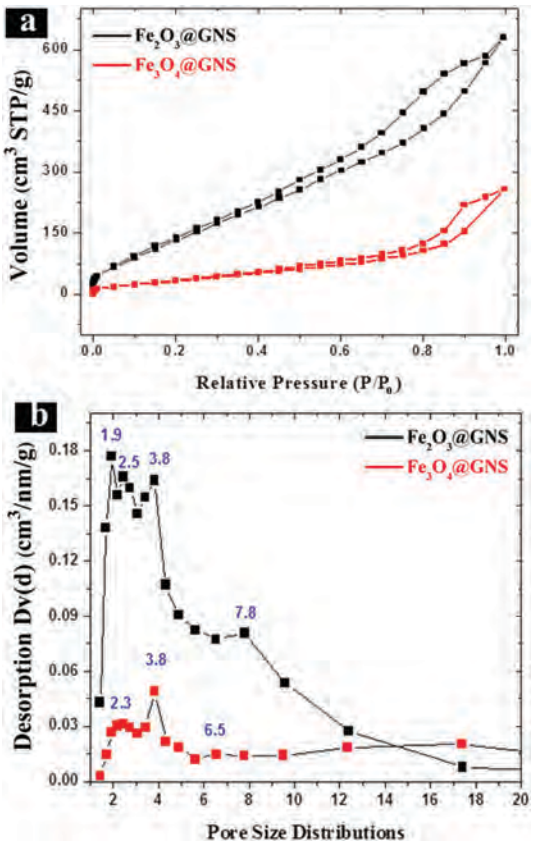

Fig. 5 (a) N_2 sorption/desorption isotherms of Fe_2O_3@GNS (black) and Fe_3O_4@GNS (red); and (b) Pore size distributions of Fe_2O_3@GNS (black) and Fe_3O_4@GNS (red).

Fe_3O_4@GNS are 509 and 132 $m^2\ g^{-1}$, respectively. The specific surface area of Fe_3O_4@GNS is smaller than that of Fe_2O_3@GNS because of the high-temperature treatment. During the annealing process, some functional groups were removed. The pores between reduced graphene and the pores in graphene with iron oxide vanished. The pore volumes of Fe_2O_3@GNS and Fe_3O_4@GNS are 0.974 and 0.398 cc g^{-1}, respectively, and the pore size distributions are 1.9, 2.5, 3.8, and 7.8 nm for Fe_2O_3@GNS and 2.3, 3.8 and 6.5 nm for Fe_3O_4@GNS.

Because of the unique nanostructure, iron oxide@GNS is a suitable anode in lithium-ion batteries, and galvanostatic discharging/charging experiments were carried out to evaluate the electrochemical performance. The first discharge capacities of Fe_2O_3, Fe_3O_4, Fe_2O_3@GNS, and Fe_3O_4@GNS were 1100, 1248, 1350, and 1700 mA h g^{-1}, respectively, at a rate of C/5 and the reversible capacities were 739, 684, 843, and 844 mA h g^{-1}, respectively, during the first charging process (Fig. 6a). The excellent lithium storage capability is related to the desirable porous texture of iron oxide coated with graphene and Li atoms can easily form semi-metallic clusters. The large specific surface area gives rise to a large irreversible capacity due to the decomposition of the electrolyte and the formation of the solid/electrolyte interphase (SEI) films at the electrode/electrolyte interface.[33,34] The rate performance of Fe_2O_3, Fe_2O_3@GNS, and Fe_3O_4@GNS is presented in Fig. 6b. The reversible capacities of Fe_2O_3, Fe_3O_4, Fe_2O_3@GNS, and Fe_3O_4@GNS are stable at 258, 174, 390, and 492 mA h g^{-1}, respectively, after 35 cycles at a rate of C/5. The high-rate cycling performance of Fe_2O_3@GNS and Fe_3O_4@GNS is very stable. For example, after 30 cycles, the retention of the reversible capacity at 10C is nearly 100% and stable at 100 and 92 mA h g^{-1} for Fe_2O_3@GNS and Fe_3O_4@GNS, respectively. The cycling voltammetry, Nyquist curves and coulombic efficiency of Fe_2O_3@GNS and Fe_3O_4@GNS are shown in Fig. S4–S6 (ESI†). In Fig. S4 (ESI†), in the first cathodic scan of Fe_2O_3@GNS and Fe_3O_4@GNS electrode, the strong reduction peaks were observed at 0.47 V and 0.57 V due to the electrochemical reduction of Fe^{3+} and Fe^{2+} to Fe^0. In the subsequent cycles, the obvious peaks at 0.47 V and 0.57 V were shifted to 0.9 V and 0.8 V due to the polarization. In the first anodic scan, three broad peaks were recorded at 1.6 V, 1.7 V and 1.86 V assignable to the oxidation of Fe^0 to Fe^{2+} and Fe^{3+}, respectively. In the subsequent cycles, however, the peak at 1.86 V is hardly observed, indicating that the redox cycle between Fe^0 and Fe^{2+} would be the major process. Overall, the integrated areas of both cathodic and anodic scans of Fe_3O_4 electrode were substantially decreased in three cycles, indicating the electrochemical irreversibility. From Fig. S5 (ESI†), it can be concluded that Fe_2O_3@GNS is more resistant than Fe_3O_4@GNS because the functional groups exist in the Fe_2O_3@GNS sample. Moreover, the coulombic efficiency is more than 95% after 35 cycles, as shown in Fig. S6 (ESI†). It is believed that the iron oxide@GNS samples have several small porous iron oxide nanorods and graphene sheets, which are responsible for the

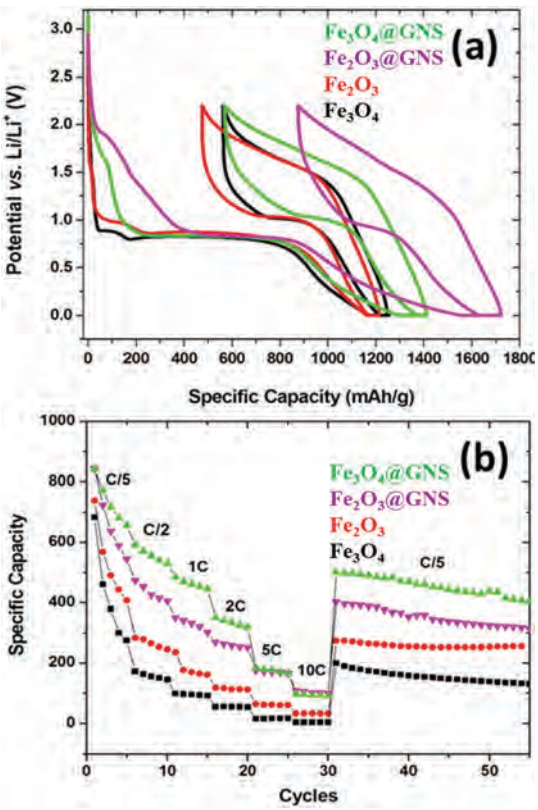

Fig. 6 (a) First charge/discharge profiles of Fe_2O_3 (red), Fe_3O_4 (black), Fe_2O_3@GNS (pink), and Fe_3O_4@GNS (green). (b) Rate performance of Fe_2O_3 (red), Fe_3O_4 (black), Fe_2O_3@GNS (pink), and Fe_3O_4@GNS (green).

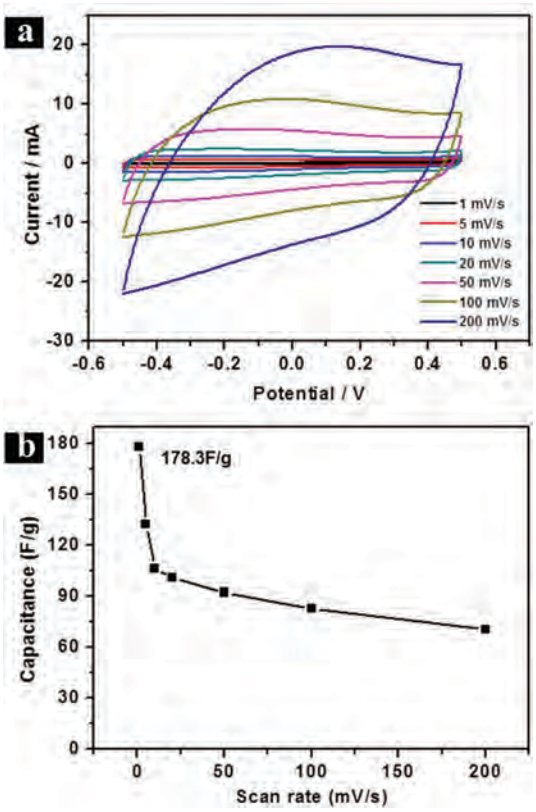

Fig. 7 (a) CV curves of Fe_3O_4@GNS electrode in the two-electrode system and (b) variation of capacitance of Fe_3O_4@GNS plotted as a function of sweep rates in 5 M KCl.

excellent Li insertion. However, it should be noted that the larger irreversible capacity is the main drawback of the materials. The long-term stability of Fe_3O_4@GNS is shown in Fig. S7 (ESI†), which shows that Fe_3O_4@GNS is relatively stable after 50 cycles.

The electrochemical performance of Fe_3O_4@GNS was characterized by the cyclic voltammetry (CV) technique in the two-electrode configuration. Fig. 7 shows the CV curves of Fe_3O_4@GNS in 5 M KCl solution at sweep rates varying from 1 to 200 mV s^{-1} in the potential range from −0.5 to 0.5 V. The CV curves of Fe_3O_4@GNS, as shown in Fig. 7a, maintain a rectangular shape even at a sweep rate as high as 200 mV s^{-1}, indicating their good capacitor behaviors. The deviation from regular rectangular shape might result from the inherent resistivity of the Fe_3O_4 electrode. The CV measurement was also used to calculate the specific capacitance of Fe_3O_4@GNS. The capacitance was plotted as a function of voltage sweep rate. Fig. 6b presents the capacitance of Fe_3O_4@GNS at different voltage sweep rates; it shows a capacitance of 178 F g^{-1} at a sweep rate of 1 mV s^{-1}. The Fe_3O_4@GNS electrode presents a dramatic decay in the capacitance with an increase in the sweep rate from 1 to 10 mV s^{-1}, but from 20 to 200 mV s^{-1}, the capacitance remains relatively stable. At a low sweep rate, ions have enough time to diffuse into the inner surface of the electrode materials, whereas at a high sweep rate, ions can only penetrate into the electrode materials with large pores, which indicates that only parts of the pores of the electrode materials take part in the electrochemical processes. As a result, the capacitance decreases with an increase in sweep rate.[35]

The material was also evaluated as electrode materials in supercapacitors *via* a galvanostatic charge/discharge technique. As shown in Fig. 8a, in the two-electrode system, the performance of Fe_3O_4@GNS is evaluated by galvanostatic charging/discharging at different current densities. The capacitance of the cell can be estimated from the charging/discharging curves using the equation $C = 2\Delta It/mV$. The specific capacitance of Fe_3O_4@GNS at a current density of 1 A g^{-1} is 68.2 F g^{-1}. The long-cycle lifetime of a supercapacitor is important in practice. Since Fe_3O_4@GNS delivered the best electrochemical performance, the electrochemical stability was investigated by examining the electrochemical cycling stability at a current density of 10 A g^{-1}. Fig. 8b shows the capacitance retention of Fe_3O_4@GNS after 10 000 cycles, and 77.7% of the specific capacitance was retained, providing evidence of good stability and long lifetime.

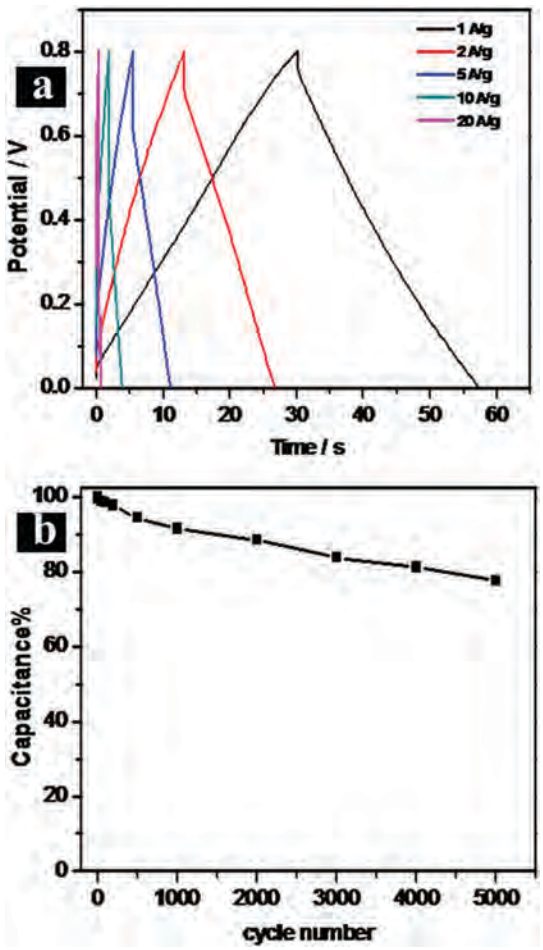

Fig. 8 (a) Galvanostatic charging/discharging curves of Fe_3O_4@GNS at different current densities and (b) cycling life tests conducted on Fe_3O_4@GNS at 10 A g^{-1}.

Conclusions

Nanocomposites composed of graphene-coated porous Fe_2O_3 and Fe_3O_4 nanorods were prepared from FeOOH@GO colloids *via* an electrostatic self-assembly method. The electrochemical properties pertaining to the application in lithium-ion batteries and supercapacitors were determined. As anode materials in lithium-ion batteries and supercapacitors, Fe_3O_4 nanorods@GNS delivered improved and stable performance compared to raw iron oxide nanoparticles. GNS not only eases the volume change of Fe_3O_4 during charging/discharging, but also increases the electrical conductivity of the hybrid materials, resulting in an improved electrochemical performance.

Experimental

Materials

$FeCl_3$ was obtained from Aladdin and hydrazine was purchased from Alfa Aesar. Natural flake graphite powder and sodium nitrate ($NaNO_3$) were obtained from Sigma-Aldrich. Potassium permanganate ($KMnO_4$) and sulfuric acid (H_2SO_4) were purchased from China National Medicines Corporation Ltd.

Synthesis of graphene oxide (GO)

GO was prepared by the oxidation of natural flake graphite powder using the Hummers method.[32]

Synthesis of Fe_2O_3@GNS and Fe_3O_4@GNS nanocomposite

In a typical synthesis, 150 ml of 0.05 mol L^{-1} $FeCl_3$ aqueous solution was hydrolyzed at 80 °C for 12 h to obtain uniform spindle-shaped FeOOH nanorods, and 100 mg of GO was dispersed in 1000 ml of water under sonication to form a 0.1 mg ml^{-1} homogeneous GO solution. Furthermore, 150 ml of FeOOH

nanorods solution was then dispersed in 1000 ml of water and mixed with the GO solution to form GO-coated FeOOH colloids by electrostatic self-assembly technique. After centrifugation, the samples were freeze-dried at −30 °C for 48 h to obtain FeOOH@GO nanorods. To prepare the graphene-coated Fe_2O_3 nanocomposite (Fe_2O_3@GNS), FeOOH@GO was reduced by hydrazine. To prepare the Fe_3O_4@GNS nanocomposite, Fe_2O_3@GNS was annealed at 450 °C for 2 h in Ar to reduce the Fe_2O_3 spindle to Fe_3O_4 *in situ*.

Characterization

The morphologies of the samples were observed *via* field-emission scanning electron microscopy (FE-SEM). The microstructures of the samples were investigated *via* transmission electron microscopy (TEM) using a JEM-1011 system at an acceleration voltage of 100 kV and *via* high-resolution transmission electron microscopy (HRTEM) using a FEI G2 S-Twin system operating at 200 kV. The phase structures of the samples were analyzed by X-ray diffraction (XRD) using a D8 advance X-ray diffractometer with Cu Kα radiation operating at 40 kV and 200 mA. The thermal stability of the samples was measured by thermogravimetric analysis (TGA) under an air flow at a heating rate of 10 °C min^{-1} using TA Instruments SDT Q600. The vibrational property of the samples was characterized *via* Raman spectroscopy (T6400, excitation-beam wavelength: 514.5 nm). The porosity properties of the samples were measured by nitrogen adsorption/desorption at 77 K using a Quantachrome Autosorb-1C-MS analyzer.

Electrochemical measurement

Lithium-ion battery measurement

The electrochemical experiments were carried out using 2032 coin-type cells. The working electrodes were prepared by mixing MPGF, carbon black (C-NERGY SUPER C65, Timcal), and polyvinylidene difluoride (PVDF, Solef 5130, Solvay) with a weight ratio of 80 : 10 : 10 and pasting the mixture onto Cu foils (Schlenk Metallfolien GmbH & Co.). A lithium foil (Aldrich) was used as the counter electrode. The electrolyte consisted of a solution of 1 M $LiPF_6$ in ethylene carbonate (EC)/dimethyl carbonate (DMC) (1 : 1 by volume) obtained from Merck Chemicals (SelectiLyte LP30). The cells were assembled in an argon-filled glovebox with less than 1 ppm moisture and oxygen. The electrochemical properties were determined in the voltage range between 0.01 and 3.0 V by the galvanostatic charging/discharging technique.

Supercapacitor measurement

The electrochemical properties of Fe_3O_4@GNS were determined using a two-electrode system at room temperature. The working electrode was prepared by mixing Fe_3O_4@GNS (80 wt%), carbon nanotubes (20–40 nm, 10 wt%), and polyvinylidene difluoride (PVDF, Solef 5130, Solvay, 10 wt%) and pressed at a pressure of 10 MPa to form a pellet with a diameter of 1 cm. The weight of the active material was 10 mg and the electrolyte was a 5 M KCl aqueous solution. The electrochemical properties were evaluated by cyclic voltammetry (CV), galvanostatic charging/discharging, and electrochemical impedance spectroscopy (EIS) measurements with an EC-LAB VMP3 (BioLogic Science Instruments). The CV curves were acquired in the potential window between −0.5 V and 0.5 V at different scanning rates from 1 to 200 mV s^{-1}. The galvanostatic charging/discharging experiments were performed between 0 and 0.8 V at current densities from 1 to 20 A g^{-1}.

Conflicts of interest

There are no conflicts to declare.

Acknowledgements

This study was supported by the National Natural Science Foundation of China (51303170), the National Science Centre, Poland, Grant No. UMO-2015/18/E/ST8/00291 and City University of Hong Kong Applied Research Grant (ARG) No. 9667122.

Notes and references

1 M. Armand and J. M. Tarascon, *Nature*, 2008, **451**, 652.
2 B. Dunn, H. Kamath and J. M. Tarascon, *Science*, 2011, **334**, 928.
3 J. Chen, L. Xu, W. Li and X. Gou, *Adv. Mater.*, 2005, **17**, 582.
4 J. Kim, M. K. Chung, B. H. Ka, J. H. Ku, S. Park, J. Ryu and S. M. Oh, *J. Electrochem. Soc.*, 2010, **157**, A412.
5 Z. S. Wu, W. C. Ren, L. Wen, L. B. Gao, J. P. Zhao, Z. P. Chen, G. M. Zhou, F. Li and H. M. Cheng, *ACS Nano*, 2010, **4**, 3187.
6 N. Kang, J. H. Park, J. Choi, J. Jin, J. Chun, I. G. Jung, J. Jeong, J. G. Park, S. M. Lee, H. J. Kim and S. U. Son, *Angew. Chem., Int. Ed.*, 2012, **51**, 6626.
7 W. M. Zhang, X. L. Wu, J. S. Hu, Y. G. Guo and L. J. Wan, *Adv. Funct. Mater.*, 2008, **18**, 3941.
8 Y. M. Sun, X. L. Hu, W. Luo and Y. H. Huang, *ACS Nano*, 2011, **5**, 7100.
9 Y. Idota, T. Kubota, A. Matsufuji, Y. Maekawa and T. Miyasaka, *Science*, 1997, **276**, 1395.
10 Y. Wu, Y. Wei, J. Wang, K. Jiang and S. Fan, *Nano Lett.*, 2013, **13**, 818.
11 D. F. He, L. Li, F. J. Bai, C. Zha, L. M. Shen, H. H. Kung and N. Z. Bao, *Chem. – Eur. J.*, 2016, **22**, 4454.
12 S. L. Yang, C. Y. Cao, G. Li, Y. B. Sun, P. P. Huang, F. F. Wei and W. G. Song, *Nano Res.*, 2015, **8**, 1339.
13 G. M. Zhou, D. W. Wang, P. X. Hou, W. S. Li, N. Li, C. Liu, F. Li and H. M. Cheng, *J. Mater. Chem.*, 2012, **22**, 17942.
14 B. Wang, J. S. Chen, H. B. Wu, Z. Wang and X. W. Lou, *J. Am. Chem. Soc.*, 2011, **133**, 17146.
15 Z. S. Wu, G. M. Zhou, L. C. Yin, W. C. Ren, F. Li and H. M. Cheng, *Nano Energy*, 2012, **1**, 107.
16 F. Han, D. Li, W. C. Li, C. Lei, Q. Sun and A. H. Lu, *Adv. Funct. Mater.*, 2013, **23**, 1692.
17 Y. Li, C. L. Zhu, T. Lu, Z. P. Guo, D. Zhang, J. Ma and S. M. Zhu, *Carbon*, 2013, **52**, 565.

18 L. W. Ji, O. Toprakci, M. Alcoutlabi, Y. F. Yao, Y. Li, S. Zhang, B. K. Guo, Z. Lin and X. W. Zhang, *ACS Appl. Mater. Interfaces*, 2012, **4**, 2672.
19 C. N. He, S. Wu, N. Q. Zhao, C. S. Shi, E. Z. Liu and J. J. Li, *ACS Nano*, 2013, **7**, 4459.
20 T. Muraliganth, A. V. Murugan and A. Manthiram, *Chem. Commun.*, 2009, 7360.
21 H. Liu, G. X. Wang, J. Z. Wang and D. Wexler, *Electrochem. Commun.*, 2008, **10**, 1879.
22 W. M. Zhang, X. L. Wu, J. S. Hu, Y. G. Guo and L. J. Wan, *Adv. Funct. Mater.*, 2008, **18**, 3941.
23 Y. Z. Piao, H. S. Kim, Y. E. Sung and T. Hyeon, *Chem. Commun.*, 2010, **46**, 118.
24 C. M. Ban, Z. C. Wu, D. T. Gillaspie, L. Chen, Y. F. Yan, J. L. Blackburn and A. C. Dillon, *Adv. Mater.*, 2010, **22**, E145.
25 W. Wei, S. B. Yang, H. X. Zhou, I. Lieberwirth, X. L. Feng and K. Müllen, *Adv. Mater.*, 2013, **25**, 2909.
26 P. Lian, X. Zhu, H. Xiang, Z. Li, W. Yang and H. Wang, *Electrochim. Acta*, 2010, **56**, 834.
27 L. Li, Y. Dou, L. Wang, M. Luo and J. Liang, *RSC Adv.*, 2014, **4**, 25658.
28 M. Liu and J. Sun, *J. Mater. Chem. A*, 2014, **2**, 12068.
29 T. Z. Liu, X. Zhang, B. Li, J. Ding, Y. Liu, G. Li, X. Meng, Q. Cai and J. Zhang, *RSC Adv.*, 2014, **4**, 50765.
30 A. Mahmood, R. Zou, Q. Wang, W. Xia, H. Tabassum, B. Qiu and R. Zhao, *ACS Appl. Mater. Interfaces*, 2016, **8**, 2148.
31 S. S. Raut and B. R. Sankapal, *New J. Chem.*, 2016, **40**, 2619.
32 C. H. Chen and L. P. Hummers, *J. Am. Chem. Soc.*, 1958, **80**, 1339.
33 N. A. Kaskhedikar and J. Maier, *Adv. Mater.*, 2009, **21**, 2664.
34 C. D. Liang, Z. J. Li and S. Dai, *Angew. Chem., Int. Ed.*, 2008, **4**, 73696.
35 K. Wang, Y. Wang, Y. Wang, E. Hosono and H. Zhou, *J. Phys. Chem. C*, 2009, **113**, 1093.